Inorganic Chemistry Communications xxx (xxxx) 111560

Contents lists available at ScienceDirect

Inorganic Chemistry Communications

journal homepage: www.elsevier.com/locate/inoche

Short communication

h-BN nanosheet-modified Ag_2WO_4 nanocomposite for improved photocatalytic dye removal: Insights into catalyst stability and reusability

Bachir Yaou Balarabe [a,*], Prasenjit Maity [a,*], Antonio Carlos S.C. Teixeira [b], Samuel Ayodele Iwarere [c]

[a] School of Engineering and Technology, National Forensic Sciences University, Sector-09, Gandhinagar 382007, India
[b] Research Group in Advanced Oxidation Processes (AdOx), Chemical Systems Engineering Center, Department of Chemical Engineering, Escola Politécnica, University of São Paulo, Av. Prof. Luciano Gualberto, tr. 3, 380, São Paulo, SP, Brazil
[c] Department of Chemical Engineering, Faculty of Engineering, Built Environment and Information Technology, University of Pretoria, Private Bag X20 Hatfield, Pretoria 0028, South Africa

ARTICLE INFO

Keywords:
BN/Ag_2WO_4
Photocatalyst
Dye degradation
Boron nitrite
Visible light
Recycle

ABSTRACT

Hexagonal boron nitride (h-BN)/Ag_2WO_4 nanocomposite photocatalyst was successfully synthesized using a simple wet chemical approach. Various spectroscopic, microscopic and gravimetric techniques were employed to examine the nanocomposite's structural, morphological, and optical properties. The catalyst showed excellent photocatalytic efficiency for degradation of Indigo Carmine (IC) dye under visible light irradiation with high catalyst stability and hence long reusability. A comprehensive evaluation and comparison of photocatalytic performance was accomplished where we examined the photocatalytic performance of several boron-nitride (BN-based) composites for their ability to degrade various pollutants. As a result, the composites demonstrated variable quantum yields (QY), space–time yields (SY), figures of merit (FOMs), and kinetic reaction rates. As a result of the efficient utilization of photons and effective promotion of photocatalytic reactions, the BN/Ag_2WO_4 nanocomposite exhibited the highest metrics performance values. A plausible reaction mechanism was also demonstrated.

1. Introduction

Water pollution through contamination of organic dye molecules disposed by various industries is a serious environmental issue. The majority of hazardous substances are non-biodegradable and mutagenic causing eco-toxicological problems. These dyes can obstruct both sunlight penetration and oxygen dissolution, which are very necessary for aquatic life [1]. The strategies adopted for cleaning dye contaminated water bodies are broadly includes separation through adsorption and catalytic dye degradation under visible light (sunlight) irradiation [2,3]. A variety of semiconductor photo catalysts have been widely studied in last few decades with the objective of developing a highly efficient low-cost technique which can harness natural sunlight for the said process. The nano-photocatalysts based on engineered semiconductors nanoparticles are found most promising material for dye degradation under suitable wavelength light [4–12]. The abundance of solar light on earth surface triggers the necessity of developing band gap tuned semiconductor-based nano-photocatalysts as low-cost technology for dye degradation. Silver (Ag) based compounds are mostly low band gap semiconductors and hence many of those have been demonstrated as efficient photo catalysts under visible-light irradiation [13,14]. Among them silver chromate/molybdate/tungstate {Ag_2MO_4 (M = Cr, Mo, W)} are a group of promising material for their application potential as photocatalysts and other opto-electrical devices [15–26]. Ag_2WO_4 is a low band (2.4 eV) semiconductor which may exists in three crystal forms namely α, β and γ. The α-Ag_2WO_4 is having hexagonal structure and more stable than other two forms. However, one serious limitation of usingAg_2WO_4 and most Silver based photocatalysts is their slow degradation to metallic Silver (Ag) under prolonged light exposure and hence diminished catalytic activity [27,28]. To overcome this issue, a variety of solid supported heterogeneous photocatalysts have been developed with improved photo stability, long catalyst lifetime, improved reusability and sometimes with improved electron hole separation efficiency [29–32]. Along with the use of well-known metal oxide-based supports (TiO_2, ZnO, Fe_3O_4, SiO_2, Al_2O_3), the use of carbon-based planer and layer materials like, Graphene, Graphene oxide, Carbon Nitride have gain momentum in recent years [26,29,30,32]. Boron nitride

* Corresponding authors.
E-mail addresses: yaoubalarabe@gmail.com (B.Y. Balarabe), prasenjit.maity@nfsu.ac.in (P. Maity).

https://doi.org/10.1016/j.inoche.2023.111560
Received 1 August 2023; Received in revised form 29 September 2023; Accepted 6 October 2023
1387-7003/

is a new type of support and co-catalyst which is showing promising results for photocatalysis.

Boron nitride (h-BN) also referred as "white graphite" due to its comparable planar hexagonal structure of alternating B and N consisting of sp^2-bonded 2D layers, with a structural lattice comparable to that of graphene's C atoms with wide band gap (5 eV). It has large specific surface area, improved oxidation resistance, thermal conductivity and high stability at room temperature [33,34]. h-BN is not suitable photocatalyst due to its high band gap (can be activated by UV light with less than 300 nm wavelength) but have been demonstrated as a good support material and co-catalyst for a variety of photocatalysts. Overall, it results better separation of photogenerated charge carriers as well as a support material it facilitates a greater number of exposed active sites and the light harvesting capacity could also be greatly enhanced. h-BN support based composite photocatalysts can create electronic heterostructure, electron migration and electrostatic interaction with the active photocatalyst and through adsorption of organic dyes on the surface of the support better photocatalytic performances are realized [34].Various semiconductors including TiO_2 [35,36], BiX_n [37,38], ZnO [39], SnS_2 [40], carbon nitride [41] and also Silver based compounds [42,43] have been combined with BN, which are effective in reducing electron-hole recombination, high stability and good photocatalyst efficiency. However, to understand the real potential of 'BN' as support and co-catalyst material, there is an urgent need of further exploration with respect the ease of catalyst synthesis, stability, catalytic activity and reusability. With those objectives the present work was undertaken to develop an h-BN/Ag_2WO_4 based nanocomposite catalyst for photocatalytic degradation of an organic dye (IC) under visible light. Different photocatalytic methods can be directly compared for assessing the efficiency with which absorbed photons are converted into productive reactions, as like quantum yield (QY) and space yield (SY). In addition to providing information on the catalytic efficiency and reaction kinetics of the photocatalyst, nonetheless, it is essential to consider specific experimental conditions, such as catalyst preparation methods, pollutant concentrations, and other factors, to ensure meaningful comparisons. Hence, a detailed analysis of the photocatalytic performance of h-BN/Ag_2WO_4 nanocomposite for IC removal using performance measurements was also performed. The reaction kinetics, space yield, quantum efficiency, and figure of merit values, which are essential for process engineering and real-world applications, were addressed in this work. Furthermore, a possible mechanism governing the reaction based on the observation and previous knowledge in this field was proposed. The present study reports visible-light-driven photocatalytic degradation of cationic dyes (Indigo carmine) under visible light with h-BN/Ag_2WO_4 nanocomposite catalysts, along with a mechanistic description.

2. Experimental

2.1. Materials

All the materials and solvents were purchased from commercial sources (Finer Chemicals, India, and Sigma Aldrich, India) and used as received without further purification. Sodium Hydroxide pellets NaOH (extra pure AR, 98 %), Sodium tungstate dihydrate $Na_2WO_4{\cdot}2H_2O$ (extra pure AR, 98 %), Silver nitrate $AgNO_3$ (extra pure AR, 98 %). Hexagonal Boron nitride nano-powder, (extra pure 99.7 %) and Indigo Carmine (IC) were procured from Sigma Aldrich. Milli-Q water and spectroscopic grade solvents were used for all measurements.

2.2. Characterization

A JASCO-670 UV/VIS/NIR spectrometer (made in Japan) was used to record optical absorbance spectra. The photoemission spectra of samples were measured by using a JASCO FP 6500 instrument (made in Japan). A JASCO FT/4700 ATR spectrophotometer (made in Japan) was also used to record the FTIR spectra. Transmission electron microscope images were captured using a Talos F200i S/TEM (HRTEM-200KV) electron microscope. The device was fitted with a Bruker X Flash 6 30 EDS Detector for quantitative elemental analysis and elemental mapping. Field Emission Gun Nano Nova Scanning Electron Microscope (FEG-SEM) 450 with EDAX (FESEM) was used to capture the SEM images using 20 kV accelerating voltage. Raman spectra were recorded using Renishaw invia Raman Spectroscopy with 785 nm red LASER. A Powder X-ray diffractometer (GNR APD 2000 PRO) with a Cu-K light source was used to measure the X-ray diffraction pattern. The thermal behaviour of the catalyst was analysed using a Perkin Elmer DSC-6000 instrument at temperatures ranging from 30 to 400 °C. The Total Organic Carbon (TOC) content of dye solution was determined by an O. I. Analytical Aurora model 1030 TOC instrument. The sample elemental composition was determined by using a Shimadzu EDXRF 7000 instrument. A Thermo Scientific K-Alpha instrument with Al K radiation source was used to measure X-ray Photoelectron spectra (XPS). The Delta Flex modular fluorescence lifetime system was used to record the Time-Correlated Single-Photon Counting spectra (Model HORIBA) for calculating excited state lifetime values. AB Sciex Mass spectrometer was used for mass spectral analysis. A Micromeritics AS-AP2020 was used to measure N2 adsorption on solid, from which a Brunauer-Emmett-Teller (BET) specific surface area was determined.

2.3. Synthesis procedures

1.65 g of sodium tungstate and 1.70 g of silver nitrate were dissolved in 250 mL water and thoroughly mixed under stirring and then the precipitation was initiated by adding a few millilitres of sodium hydroxide to the mixture. Afterwards the whole solution was transferred to an autoclave, Ag_2WO_4 nanoparticles were formed (Scheme 1.1) [22]. As part of the exfoliation process, 1 g of boron nitride nanopowder was immersed in 10 mL of sulfuric acid and stirred continuously for 9 h. After a thorough washing was conducted until the pH reached 7 (as shown in Scheme 1.2), ultrasound was applied for 30 min, followed by 500 mL of distilled water [44]. Following the synthesis of the nanocomposite of boron nitride and silver tungstate, 300 mg of exfoliated boron nitride powders were mixed with 150 mg of Ag_2WO_4 nanoparticles in 40 mL of distilled water. After stirring the resulting mixture for 24 h at room temperature, 1 M NaOH was added to adjust the pH to approximately 7. The precipitate generated was centrifuged at 600 rpm, washed several times with deionised water and ethanol, and dried overnight at 100 °C (see Scheme 1.3).

2.4. Photocatalytic activity measurements

The photocatalytic reaction (dye degradation) was investigated using a photo-catalytic reactor equipped with a 125-watt mercury visible lamp with the emission line beginning at the UVA range (350 nm) and extends up to visible end of the spectrum (700 nm). The photocatalytic reaction was performed by adding 200 mL of an aqueous solution of IC dye with a concentration of 20 g/L to the 500 mL capacity photoreactor and 50 mg of catalyst. Before irradiation, the suspension was first magnetically stirred for 20 min in the dark to achieve an adsorption–desorption equilibrium. The progress of the reaction was followed by withdrawing 0.5 mL aliquots at regular time intervals from the flask; it was mixed with 2 mL of water and then measuring the absorbance using a spectrophotometer.

3. Results and discussion

The optical absorption spectra of BN, Ag_2WO_4 and BN/Ag_2WO_4 nanocomposite are shown in Fig. 1. Boron nitride sheets have negligible absorbance in the entire spectrum, but Ag_2WO_4 nanoparticles showed

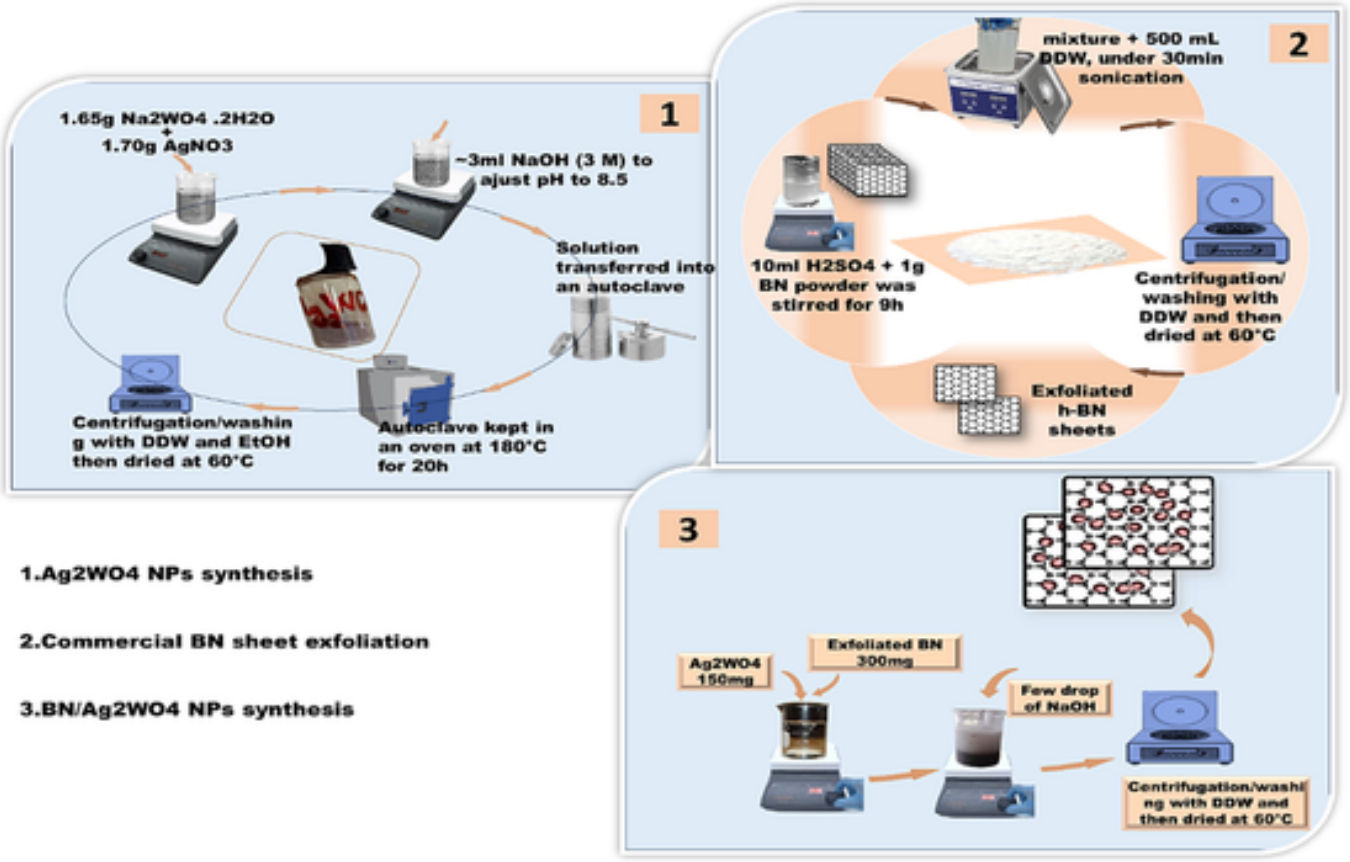

Scheme 1. Depiction of Experimental procedure for the synthesis of h-BN/Ag_2WO_4 nanocomposites.

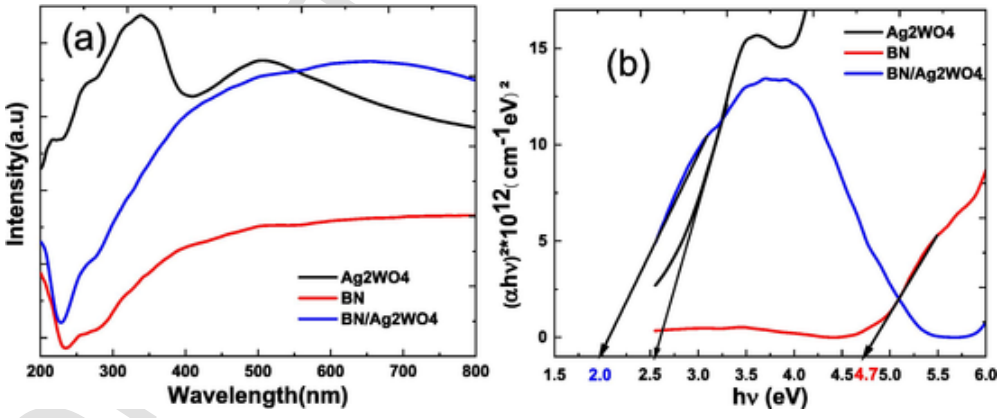

Fig. 1. (a) UV–Vis Diffuse reflectance spectra, (b) Direct band gap spectra of BN, Ag_2WO_4 and BN/Ag_2WO_4 nanocomposites.

characteristic strong light absorbance profile in the 200–800 nm region. Hence as expected the synthesized BN/Ag_2WO_4 nanocomposite has a broad absorbance profile encompassing the entire visible region of the spectrum (Fig. 1a). The bulk hexagonal boron nitride (h-BN) is a layered ultra-wide-band-gap semiconductor with an indirect band gap of 5.95 eV [35], but the one calculated based on the absorbance spectrum obtained in this experiment was 4.7 eV. The calculated absorbance of the BN/Ag_2WO_4 was 2.0 eV, which is promising because it can improve the photocatalytic activity of the as-prepared nanocomposites under visible light (Fig. 1b).

In order to calculate the valence and conduction band potentials of BN and Ag_2WO_4, band gap energies and average geometric electronegativity of the semiconductors were calculated. As explained in Equation (1) and (2) by Guo et al. , this calculation follows the specified equations, where Ee (4.5 eV) represents the energy of free electrons vs. hydrogen [45]. By calculating the geometric mean of the electronegativities of the atoms constituting the semiconductor, the χ value can be determined. Xu et al. explain that, in order to achieve this, we use the following formula (Equation (3), in which the electronegativities of atoms A and B are represented by (A) and (B), and the number of these atoms in the semiconductor are represented by exponents a and b. In equation (4), the electronegativity of each atom is determined by its first ionization Ei and electron affinity Ea [46]. By determining whether the valence and conduction bands are aligned at the interface, band offsets indicate whether electrons or holes are transferred. Electrons are the majority of charge carriers in n-type semiconductors, as opposed to holes in p-type semiconductors. BN has negative E_{CB} values, which indicate a lower energy level, making it a p-type semiconductor, while Ag_2WO_4

and BN/Ag_2WO_4 nanocomposites have positive E_{VB} and E_{CB} values, indicating n-type semiconductors [47]. These values are presented in Table 1

$$E_{VB} = (\chi - Ee) + 0.5Eg \quad (1)$$

$$E_{CB} = E_{VB} - Eg \quad (2)$$

$$\chi = \sqrt[(a+b)]{\frac{A^a * B^b}{a+b}} \quad (3)$$

$$A \text{ or } B = \frac{Ea + Ei}{2} \quad (4)$$

The solid-state photoluminescence spectra were recorded to gain a better understanding of their electronic structures by exciting all three samples using 300 nm light (Fig. 2a). BN showed no significant emission profile, however the emission peak maxima of Ag_2WO_4 was observed at 390 nm and for BN/Ag_2WO_4 at the peak gets blue shifted to 350 nm. The excited state decay profiles of all these three samples were also measured by TCSPC using 300 nm excitation source (Fig. 2b). The excited state lifetime for BN, Ag_2WO_4BN/Ag_2WO_4, were found to be 1.34 ns, 3.40 ns and 3.58 ns respectively. The increase τ value for the BN/Ag_2WO_4 photocatalyst indicates positive electron transfer from Ag_2WO_4 to BN. This effectively prevents charge carrier recombination by transferring charge carriers, subsequent photocatalytic reactions are enhanced by the active involvement of charge carriers, which leads to increased catalytic efficiency.

FT-IR spectroscopy was used to investigate the quality of the as-prepared nanoparticles as well as their intricate chemical functionalities (Fig. 3a). The presence of surface —OH groups is confirmed through broad peak at 3480 cm^{-1}. The peak at 2330 cm^{-1} indicates the presence of atmospheric O═C═O bond stretching. The tungsten oxide vibrations are found in the 1343 cm^{-1} infrared region, which corresponds to W—O stretching, bending, and lattice mode [48].The peak at 1387 cm^{-1} is caused by a B—N stretching vibration [49].The spectrum shows a weak absorption at 863 cm^{-1} induced by the asymmetric stretching vibrations of O—W—O bonds [50].

Table 1
Optical properties of the samples.

Elements	Ea (eV)	Ei (eV)	(Ea + Ei)/2	
B	0.279	8.298	4.29	
N	−0.07	14.534	7.23	
Ag	1.304	7.576	4.44	
W	0.816	7.864	4.34	
O	1.461	13.618	7.54	
Samples	χ	Eg	E_{VB}	E_{CB}
Ag_2WO_4	5.98	2.5	2.73	0.23
BN	5.57	4.7	3.42	−1.28
BN/Ag_2WO_4	5.88	2	2.38	0.38

The thermal stability of the synthesized catalysts from room temperature to 300 ˚C is illustrated in Fig. 3b. The DSC graph of BN/Ag_2WO_4 shows a sharp melting temperature of 210 ˚C. A high melting temperature can be attributed to good intermolecular cohesion, which is may be due to solid-state self-organization and the possibility of a phase transition [51].

The presence of silver (Ag—Ag bond) is also indicated by a Raman shift at 875 cm^{-1}, whereas the tungsten (W—W bond) peak at 304.35 cm^{-1} is attributed to tungsten, as shown in [52,53]. The prominent peaks at 1357.60 cm^{-1}, 875 cm^{-1}, and 304.35 cm^{-1} of the BN/Ag_2WO_4 composites provide confirmation of the presence of BN and Ag_2WO_4 nanoparticles through Raman spectral signatures (Fig. 3c).

Fig. 3d shows the Powder X-ray diffraction pattern of BN, Ag_2WO_4 and BN/Ag_2WO_4 nanocomposites. Based on the Crystallography Open Database (cod_1509984), the peaks observed at angles 30.18°, 31.49°, 32.88°, 45.09°, 54.43°, and 57.79° are related to the crystallographic planes (0 0 2), (2 3 1), (4 0 0), (4 0 2), (2 3 3) and (6 3 1) of the orthorhombic structure Ag_2WO_4 nanoparticles. There are two diffraction peaks for BN at angles 26.66° and 41.98°, corresponding to (0 0 2) and (1 1 0) crystal planes respectively. These peaks correspond well to the characteristics of hexagonal boron nitride as reported in the open database of crystallography (cod_1010602). In addition, there were no distinct peaks from other phases in the synthesized sample, indicating its high purity. Specifically, the presence of peaks at angles 32.88° and 26.66°, corresponding respectively to (4 0 0) and (0 0 2), provides irrefutable evidence that Ag_2WO_4 and BN are present in the BN/Ag_2WO_4 nanocomposite.

A scanning electron microscope analysis was used to examine the surface morphologies of the prepared samples. Fig. 4 (a–c) presents the scanning electron microscope images of BN/Ag_2WO_4 nanocomposite. The image confirms the uniform deposition of spherical shape Ag_2WO_4 nanoparticles on the surface of an irregularly shaped Boron nitride sheet. The elemental mapping analysis images in Fig. 4(d–g) shows the presence of N, Ag, W, and O elements in BN/Ag_2WO_4 nanocomposites. Furthermore, the atomic percentage of these elements is shown by the EDX analysis performed on the same image. Thus, the N, O, W, and Ag abundances are 66.86 %, 31.57 %, 1.14 %, and 0.43 %, respectively (Fig. 4h). Boron (B) is absent from both mapping and EDX analysis because it is one of the light elements with low photon energies that are difficult to analyse.

The XPS measurement of the BN/Ag_2WO_4 nanocomposite was also carried out in order to reconfirm the elemental compositions and more importantly to determine the oxidation state of the targeted elements. Fig. 5 shows the sample's narrow scan spectra for B1s, N1s, Ag3d, W4f, and O1s and C1s orbitals and the XPS survey (wide scan spectra) reveals the presence of all elements. The presence of Boron and Nitrogen in the sample was confirmed by the spectra of B1s peak at 192.33 eV and N1s peak at 399.85 eV. This is in agreement with the literature on BN mate-

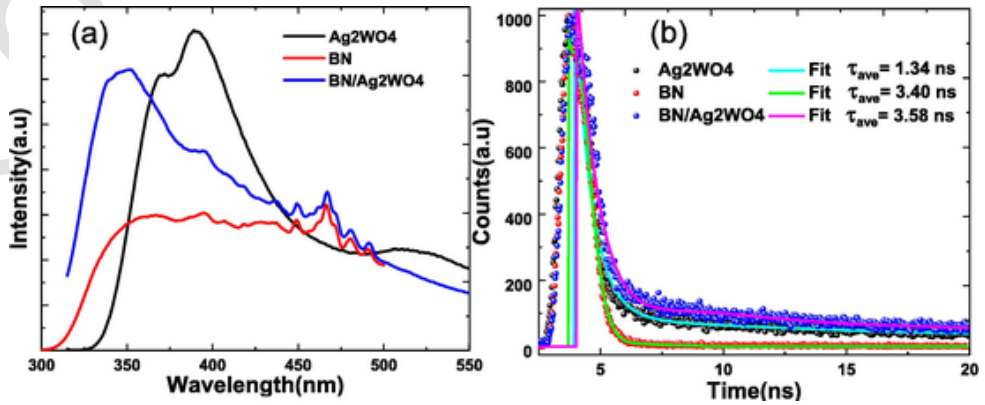

Fig. 2. Photoluminescence spectra and (a) Excited state decay profiles of BN, Ag_2WO_4 and BN/Ag_2WO_4nanocomposites.

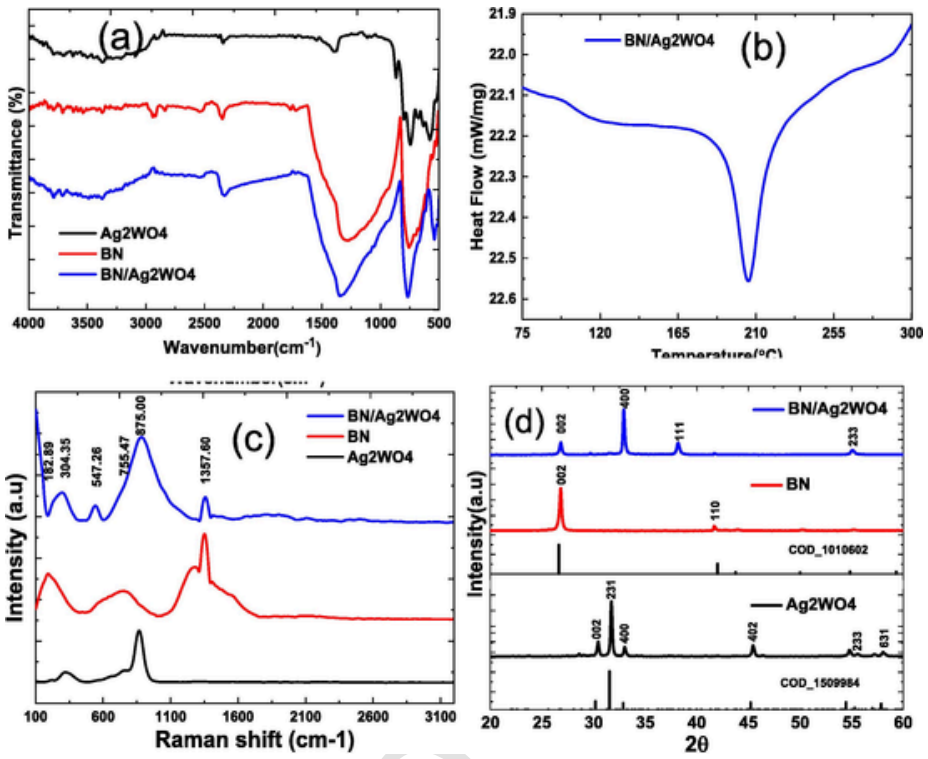

Fig. 3. (a)-Fourier Transform Infrared (FT-IR) spectra of the nanocomposites, (b)-DSC profiles of graph of BN/Ag_2WO_4nanocomposites, (c)-Raman spectra and (d) P-XRD pattern of BN, Ag_2WO_4, and BN/Ag_2WO_4 nanocomposites.

rials [54,55]. Ag3d peaks at 373.7 eV and 367.7 eV are assigned to $Ag3d_{3/2}$ and $Ag3d_{5/2}$, respectively, which are the oxidation stage of Ag (+1) [56]. At 36.65 eV and 35.5 eV, the W4f peak corresponds to the binding energies of W (+6) in WO_4^{2-} [57].

It is believed that the peak of O1s at 530.1 eV is the result of the W–O in WO_4^{2-}[58]. As a result of external carbon contamination, the C–O from adsorbed CO_2 is responsible for the C1s peaks located at 285 eV.

Materials science relies heavily upon the BET analysis since it provides information concerning surface properties [59–61]. Fig. S1 illustrates the BET analysis of nanocomposites. In processes such as the photodegradation of indigo carmine dye, it is extremely important to know the surface properties of Ag_2WO_4, BN, and BN/Ag_2WO_4. In spite of its moderate surface area, Ag_2WO_4 possesses a sufficient number of active sites, making it effective in dye degradation. In contrast, BN, with its greater surface area, exhibits the greatest ability to adsorb and degrade dyes (Table 2). It is particularly interesting to note that the BN/Ag_2WO_4 combination will be particularly effective at degrading dyes. A joint action between these two materials produces increased surface area and improved performance.

4. Photocatalytic experiment

The photocatalytic performance of the as-prepared nanoparticles for the degradation of indigo carmine under visible light was investigated. As previously stated, the reaction was carried out by taking a certain amount of dye solution and 100 mg of catalysts. Before irradiation, the suspension was sonicated for 10 min and then placed in the dark for another 10 min. The reaction was then monitored by withdrawing 1 mL aliquots from the flask at regular time intervals, mixing them with 1 mL of deionized water, and measuring the absorbance with a spectrophotometer [8]. In equation (5), the degradation efficiency of the photocatalyst is defined as follows:

$$\text{Degradation efficiency}\,(\%) = \frac{C0 - Ct}{C0} \times 100\% \quad (5)$$

Where C0 represents the dye concentration at adsorption equilibrium and Ct represents the dye residual concentration at different illumination intervals.

4.1. Effect of pH

Photocatalytic processes require the pH level of the solution to be considered and adjusted in order to be effective [62–64]. The reaction was carried out by taking (100 ppm, 200 mL) dye solution and 100 mg of catalysts at different pH. Based on the pHpzc (point of zero charge) level of BN and Ag_2WO_4 nanoparticles, which is approximately 3–4, indicating a neutral surface charge at this pH level [65,66]. This study explored a pH range of 2, 3, 5, 7, 9, and 12 (Fig. S2). For designing photocatalytic experiments with various pH levels, it is essential to understand pHpzc. In acidic conditions (pH 2 and 3), the nanoparticles become positively charged, which enhances the adsorption of anionic dyes. While electrostatic interactions are less significant at pH 5 (near pHpzc), photocatalytic degradation still occurs due to the intrinsic catalytic activity of the nanoparticles. When pH 7 (neutral) is reached, electrostatic forces are reduced, but photocatalytic degradation continues through other mechanisms as the surface charge is close to neutral. The nanoparticles are negatively charged under alkaline conditions, which can decrease dye adsorption, but photocatalytic degradation continues as a result of their catalytic properties.

4.2. Effect of time

The experimental condition was fixed at: 100 ppm, 200 mL of dye solution, 100 mg of catalysts at different and pH solution 2. As shown in Fig. 6 (a–c), increasing the time gradually reduced the absorbance peak. After 15 mins, the IC removable for BN, BN/Ag_2WO_4, and Ag_2WO_4 was

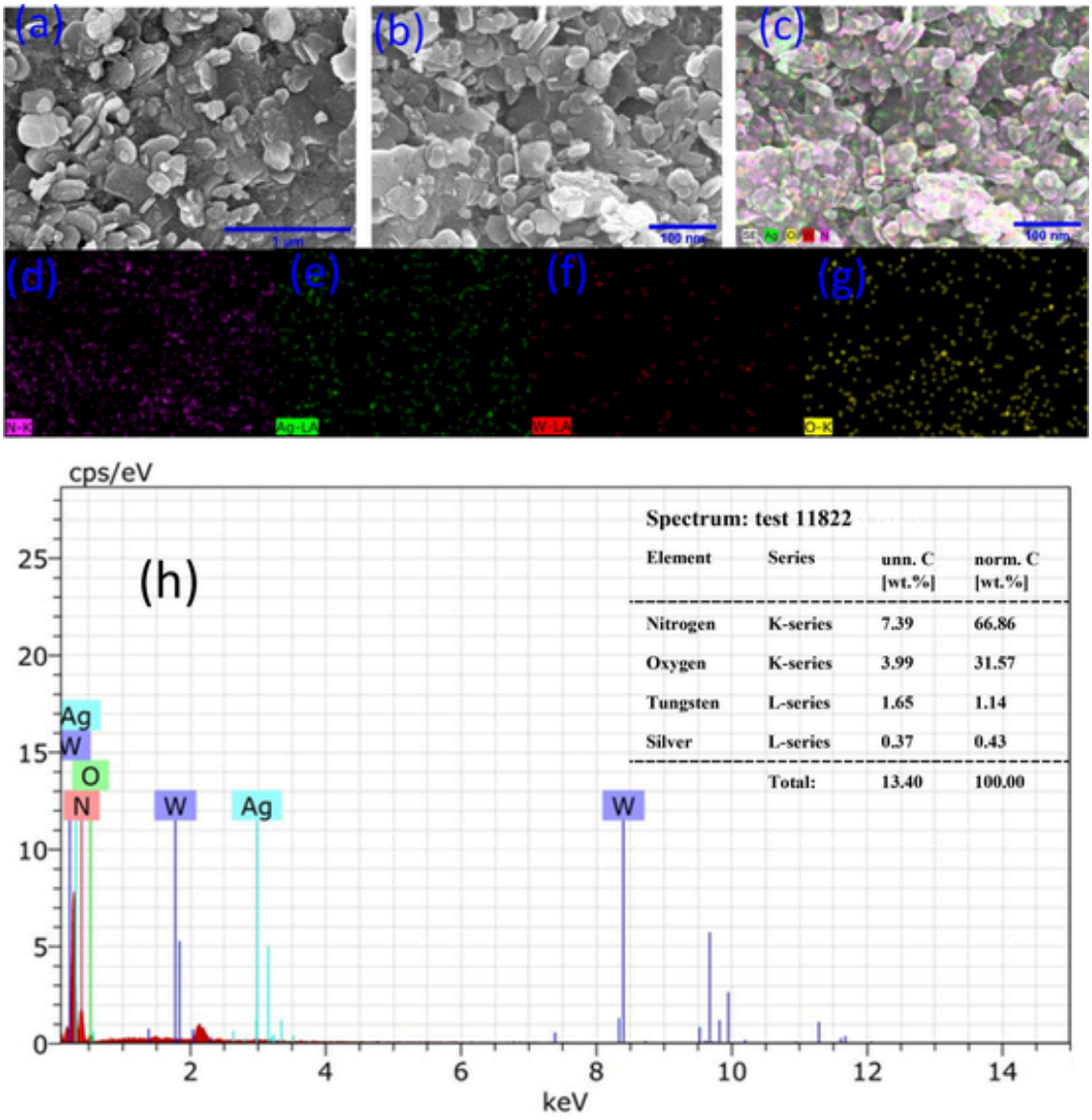

Fig. 4. (a–c) FE-SEM images of BN/Ag_2WO_4 nanocomposites, (d–g) chemical mapping for elements N, Ag, W and O respectively, (h) EDX spectrum and elemental compositions of BN/Ag_2WO_4 nanocomposites.

approximately 98 %, 94 %, and 53 %, respectively. A mass spectral analysis confirms the same findings (Fig. S3). The pseudo-first-order kinetics and kinetic rate constant are calculated using the equation below (Eq. (6)).

$$-\ln\left(C_t/C_0\right) = kt \quad (6)$$

The curve is nearly linear in shape. According to the linear logarithm plot versus irradiation time, the photodegradation reaction approximates first-order kinetics with a rate constant (K) = 0.08 min^{-1}. Based on these 'k' values, it is possible to conclude that the nanoparticles have excellent photocatalytic activity (Fig. 6d).

Photocatalytic performance has been evaluated using quantum yield (QY), which has proven to be a useful metric. Equation (7) can be used to accurately determine the quantum yield of a photocatalytic system, allowing meticulous and efficient analysis of photocatalytic reactions. To fully understand the true efficiency of photocatalytic performance, it is necessary to consider the efficiency per mass of the photocatalyst used during operation. In recent years, spatio-temporal yield values have become an increasingly meaningful metric [67,68] (equation (8)). Taking this perspective into consideration allows for a more comprehensive and insightful evaluation of photocatalytic performance. As a further measure of the accuracy of this assessment, the researchers suggested using space yield (SY), which is based on the amount of product produced per unit mass of the photocatalyst over a specific time period [69] simplify the calculation by substituting the mass of the photocatalyst for the volume of the catalytic bed. Using this approach, direct comparisons can be made and it aligns with the concept of turnover frequency (TOF), which measures the number of pollutant molecules processed per unit time at each catalytic site within the catalytic material. Instead of considering the number of catalytic sites, the net mass of the catalyst employed in the process is considered. Using the Figure of Merit (FOM), it is possible to assess the effectiveness of a photocatalyst in promoting photocatalytic reactions. This makes SY values an easier method of comparing specific processes. Accordingly, researchers can analyze different photocatalytic systems to identify those which produce superior products or reduce pollutants more efficiently [70,71]. This allows researchers to optimize and evaluate photocatalytic processes (equation (9)).

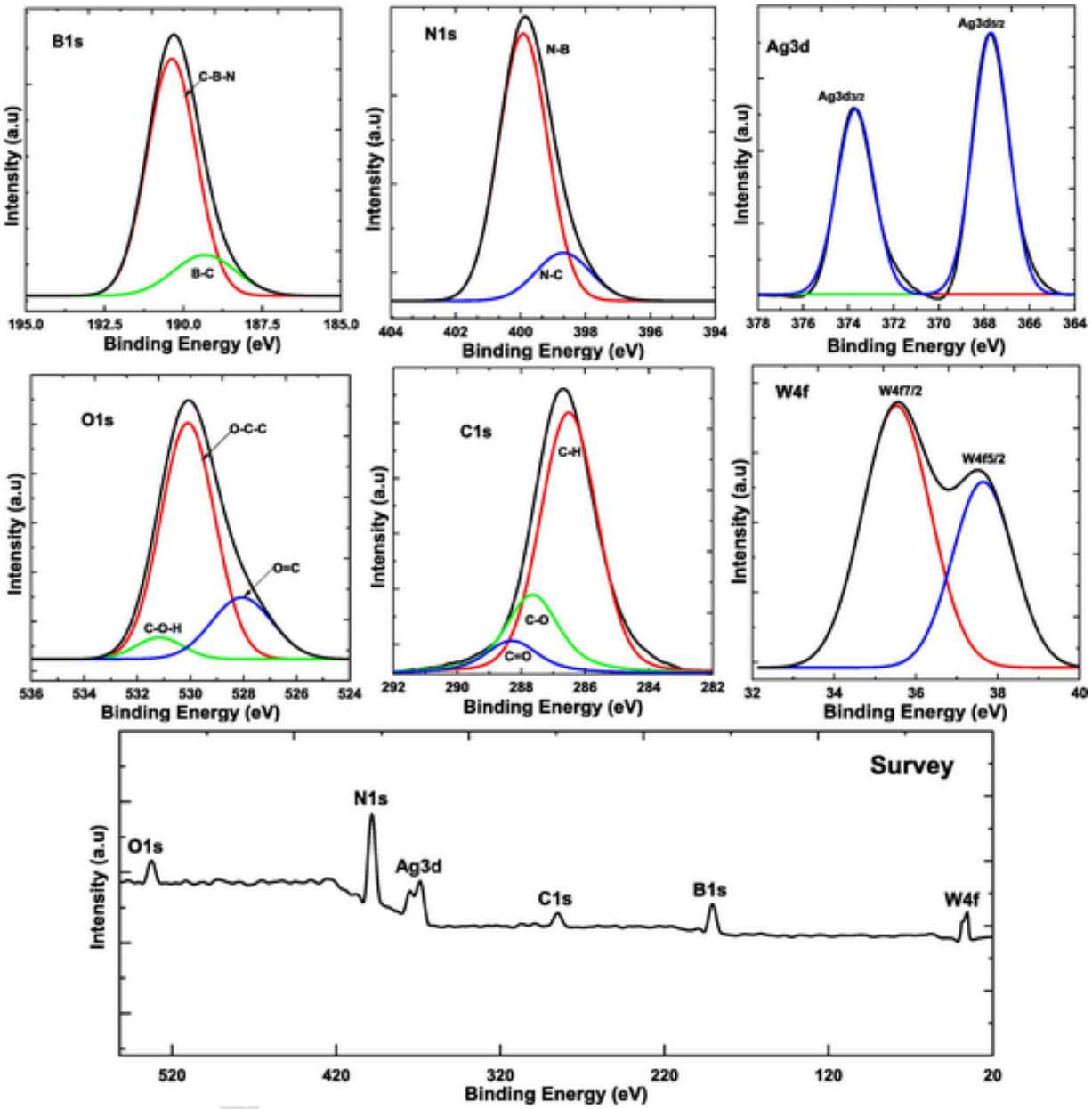

Fig. 5. XPS spectra of BN/Ag_2WO_4 nanocomposites.

Table 2
Surface area of the composites.

Samples	Surface area m^2/g
Ag_2WO_4	120.3
BN	339.42
BN/Ag_2WO_4	424.28

$$QY = \text{Decay Rate (molecule per second)} / \text{Photon flux (photon per second)} \quad (7)$$

$$SY = QY\ (\text{molecule per second}) / \text{Photocatalyst mass (mg)} \quad (8)$$

$$FOM = \text{Product obtained (L)} / \text{catalyst mass (g)} * \text{Time (h)} * \text{Energy consumption (Wh/umol)} \quad (9)$$

Different composites are compared based on quantum yield (QY), space yield (SY), figure of merit (FOM), and kinetic reaction rate. As shown in the Table 3, the composites offer a range of QY values ranging from 2.56E−09 to 1.02E−06. Accordingly, BN/Ag_2WO_4 demonstrated the highest QY, followed by BN/SnO_2, indicating that absorbed photons are most efficiently converted into photochemical reactions for the targeted pollutant, indigo carmine. Additionally, the kinetic reaction rates, expressed in umol/g/h, vary from one study to the next. A composite of BN/Bi_2-WO_6 showed a reaction rate of 1.23E+01 umol/g/h for rhodamine B. In contrast, BN/WO_3 showed a rate of 5.71E+02 umol/g/h for the same pollutant. The kinetic rates of these composites provide information regarding their catalytic efficiency and reaction kinetics. This study also revealed a significant degradation rate per unit mass of photocatalyst, with SY values ranging from 1.39E−11 to 6.23E−08 (photons^{-1} mg^{-1}), with BN/SnO_2 having the highest SY, followed by BN/Ag_2WO_4, which indicates a significant degradation rate. Also, FOM values vary from 1.85E−13 to 2.08E−08 (mol L h^{-1} g^{-1} J^{-1}), with BN/SnO_2 and BN/Ag_2WO_4 again showing the highest FOM values. Combined, these measurements provide insight into how effectively photocatalysts promote photocatalysis.

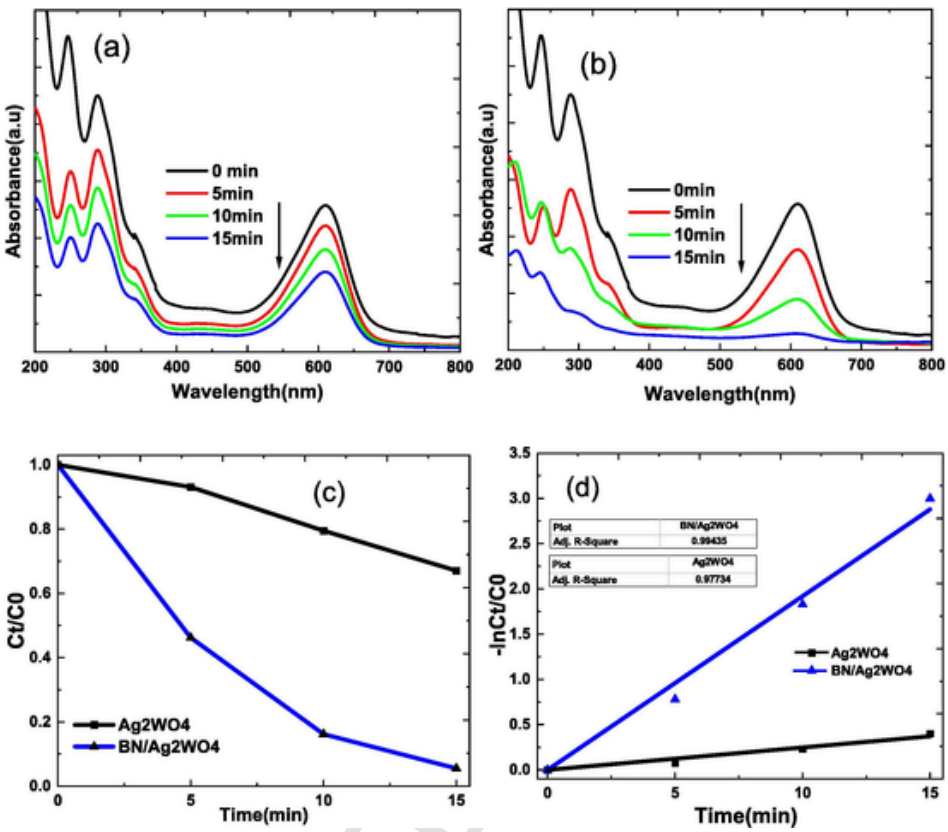

Fig. 6. Photocatalytic efficiency for Indigo carmine dye degradation using (a) Ag_2WO_4, (b) BN/Ag_2WO_4 nanocomposites under visible light. (c,d)-Photocatalytic degradation curves (C_t/C_0 vs. time) and Kinetic linear simulation curves ($-\ln(C_t/C_0)$ vs. time).

One of the most important aspects of a catalyst's practical large-scale applications is its reusability. The reusability of the photocatalyst was tested under identical conditions using visible light irradiation with IC. The catalyst was collected by centrifugation after each batch, washed repeatedly with ethanol and water, and dried before being used in the next batch of reaction. BN/Ag_2WO_4 demonstrated very good reusability up to the fourth recycle without any significant decrease in degradation efficiency while the activity and reusability of individual BN or Ag_2WO_4 showed quite poor result as demonstrated in Fig. 7 (a–d). This is due to the fact that the pollutants are only deposited on the surface of the BN nanosheet, hence for the first cycle of treatment, the degradation was very high. However, from the second to the last treatment, because the surface of the nanosheet is saturated, BN can no longer absorb pollutants. This demonstrates that the BN nanosheet alone is unstable but while combine with Ag_2WO_4nanoparticles the photodegradation as well as the stability of the nanocomposite improved (Fig. 7e).

Photocatalytic dye degradation monitored by UV–Vis spectroscopy may be overstated because the dye molecule is frequently fragmented, forming small molecules and ions that are also toxic. The ideal end product of dye degradation should be the complete oxidation of carbon dioxide and water. As a result, TOC analysis is the best way to determine whether a compound is completely mineralized or not. The TOC results revealed that the removable percentage of dye decreases significantly as reaction time increases, but this is not directly proportional to decreased optical absorption values. For instance, in the indigo carmine dye degradation study, the colour degradation was close to 100 % within 15 mins, but at the same time the TOC removal value reached only 62.56 % after 1 h of treatment (Fig. S4). This is due to that fact that instead of oxidation to H_2O and CO_2, the dye is only degraded to intermediate by-products such as aldehydes and aliphatic acids, which are far more difficult to degrade than the initial dye molecules, resulting in a low percentage of TOC removals compared to the rate of discoloration [81].

When the Ag_2WO_4 nanoparticles absorbed photon energy from the Vis-light source, the photogenerated electrons in the valance band moved to the conduction band, leaving the photogenerated holes in the valance band, as shown in Scheme 2. These electron-hole pairs will reduce and oxidize O_2 and H_2O, respectively, to produce $\cdot O_2^-$ radicals and $\cdot OH$ radicals. These radicals with a high oxidation potential can degrade pollutants to complex intermediate compounds that can then be degraded to the simpler molecules CO_2 and H_2O [82]. Boron nitride sheet acts as a pollutant immobilizer, and adsorbent, so the radicals produced by the excitation of Ag_2WO_4 can easily degrade the pollutants present nearby as boron promotes reduction reactions, while nitrogen promotes oxidation reactions, the boron in the sheet will facilitate the attraction of electrons at the nitrogen level and protons at the boron level.

5. Conclusion

In summary the study has demonstrated a facile wet chemical synthesis strategy for BN/Ag_2WO_4nanocomposite. The two materials were bonded together to create a new hybrid nanomaterial with diverse and unique properties such as high photostability and excellent UV–visible light absorbance. There is promising evidence for the degradation of pollutants using the BN/Ag_2WO_4 nanocomposite. In addition to its high quantum yield and figure of merit, the nanocomposite exhibits high efficiency in converting photons absorbed into photocatalytic reactions. In addition to its excellent performance in destroying pollutants, such as indigo carmine, it has been demonstrated to have a high QY value for degrading pollutants. Furthermore, the nanocomposite exhibits a significant space yield, indicating that the photocatalyst can effectively degrade pollutants per unit mass. BN/Ag_2WO_4 nanocomposite exhibits

Table 3
Comparative study of BN-based nanocomposites: Quantum yields, space yields, and figures of merit for pollutant degradation.

BN based composites	Targeted pollutants	Mw	Dye Conc. (g/L)	Volume (L)	Dosage (g)	Time (min)	Degrad. Eff. (%)	Lamp power (W)	Wavel. (m)	Amount of pollutant removed (moles)	Amount of pollutant removed (molecules)	Number of photons consumed	Reaction rate (umol/g/h)	QY (molecules photon^{-1})	SY (molecules photon^{-1} mg^{-1})	FOM (mol L h^{-1} g^{-1} J^{-1})	References
BN/Bi_2-WO_6	Rhodamine B	479.02	0.01	0.075	0.075	100	98.2	300	400E−7	1.54E−06	9.26E+17	3.62E+26	1.23E+01	2.56E−09	3.41E−11	5.13E−13	Li et al. [72]
BN-TiO_2	Methylene blue	319.85	0.01	0.03	0.01	200	79	300	420E−7	7.41E−07	4.46E+17	7.60E+26	2.22E+01	5.87E−10	5.87E−11	1.85E−13	Singh et al. [33]
BN/WO_3	Rhodamine B	479.02	1	0.075	0.075	180	82	300	400E−7	1.28E−04	7.73E+19	6.52E+26	5.71E+02	1.19E−07	1.58E−09	1.32E−11	Ref 19Xu et al. [73]
BN-TiO_2	Methyl orange	327.33	0.01	0.025	0.01	75	99	48	400E−7	7.56E−07	4.55E+17	4.34E+25	6.05E+01	1.05E−08	1.05E−09	7.00E−12	Nasr et al. [74]
WO_3/hBN	Rhodamine B	479.02	0.01	0.05	0.005	360	92	300	400E−7	9.60E−07	5.78E+17	1.30E+27	3.20E+01	4.44E−10	8.88E−11	2.47E−13	Gu et al. [75]
BN/SnO_2	Methyl orange	327.33	0.01	0.05	0.00125	3	92	300	400E−7	1.41E−06	8.46E+17	1.09E+25	2.25E+04	7.79E−08	6.23E−08	2.08E−08	Singh et al. [76]
SnS_2/BN sheets	Rhodamine B	479.02	0.01	0.15	0.05	210	93.7	300	420E−7	2.93E−06	1.77E+18	7.98E+26	1.68E+01	2.21E−09	4.43E−11	6.65E−13	Wu et al. [41]
BN-doped polyaniline	Methylene blue	319.85	0.01	0.1	0.02	90	93	300	365E−7	2.91E−06	1.75E+18	2.97E+26	9.69E+01	5.89E−09	2.94E−10	5.98E−12	Shahabuddin et al. [77]
	Methyl orange	327.33					95			2.90E−06	1.75E+18	2.97E+26	9.67E+01	5.88E−09	2.94E−10	5.97E−12	
TiO_2/BNNTs	Crystal violet	–	0.05	0.005	0.03	–	–	1000	300E−7	–	–	–	–	–	–	–	Weng et al. [78]
SnO_2/BNMB	Methyl orange	327.33	0.025	0.05	0.025	30	92	300	420E−7	3.51E−06	2.12E+18	1.14E+26	2.81E+02	1.86E−08	7.42E−10	2.60E−11	Wang et al. [79]
h-BN/TiO_2	Rhodamine B	479.02	0.005	0.05	0.1	20	91.2	375	365E−7	4.76E−07	2.87E+17	8.26E+25	1.43E+01	3.47E−09	3.47E−11	1.59E−12	Fu et al. [36]
	Methylene blue	319.85	0.0032				72.1			3.61E−07	2.17E+17	8.26E+25	1.08E+01	2.63E−09	2.63E−11	1.20E−12	
h-BN/ZnO	Methylene blue	319.85	0.0032	0.05	0.1	25	60	375	365E−7	3.00E−07	1.81E+17	1.03E+26	7.20E+00	1.75E−09	1.75E−11	6.40E−13	Fu et al. [40]
	Rhodamine B	479.02	0.005			25	82			4.28E−07	2.58E+17	1.03E+26	1.03E+01	2.50E−09	2.50E−11	9.13E−13	
	Methyl orange	327.33	0.01			20	21			3.21E−07	1.93E+17	8.26E+25	9.62E+00	2.34E−09	2.34E−11	1.07E−12	
	Congo red	696.65	0.007			20	38			1.91E−07	1.15E+17	8.26E+25	5.73E+00	1.39E−09	1.39E−11	6.36E−13	
BN/Ag_3PO_4	Rhodamine B	479.02	0.01	0.075	0.075	12	97	300	400E−7	1.52E−06	9.15E+17	4.34E+25	1.01E+02	2.11E−08	2.81E−10	3.52E−11	Song et al. [80]
BN/Ag_2CO_3	Rhodamine B	–	–	–	–	60	96.5	–	–	–	–	–	–	–	–	–	Wang et al. [42]
BN/Ag_2WO_4	Indigo carmine	466.36	0.1	0.2	0.1	15	94	125	420E−7	4.03E−05	2.43E+19	2.38E+25	1.61E+03	1.02E−06	1.02E−08	2.87E−09	This work

*According to the referenced study, the QY values were calculated based on the peak wavelength of light. For studies lacking precise wavelength information and lamp power, common UV light (e.g., 365 nm), visible light (e.g., 420 nm, 250 W) and a lamp power 300 W were used as reference values for performance evaluation.

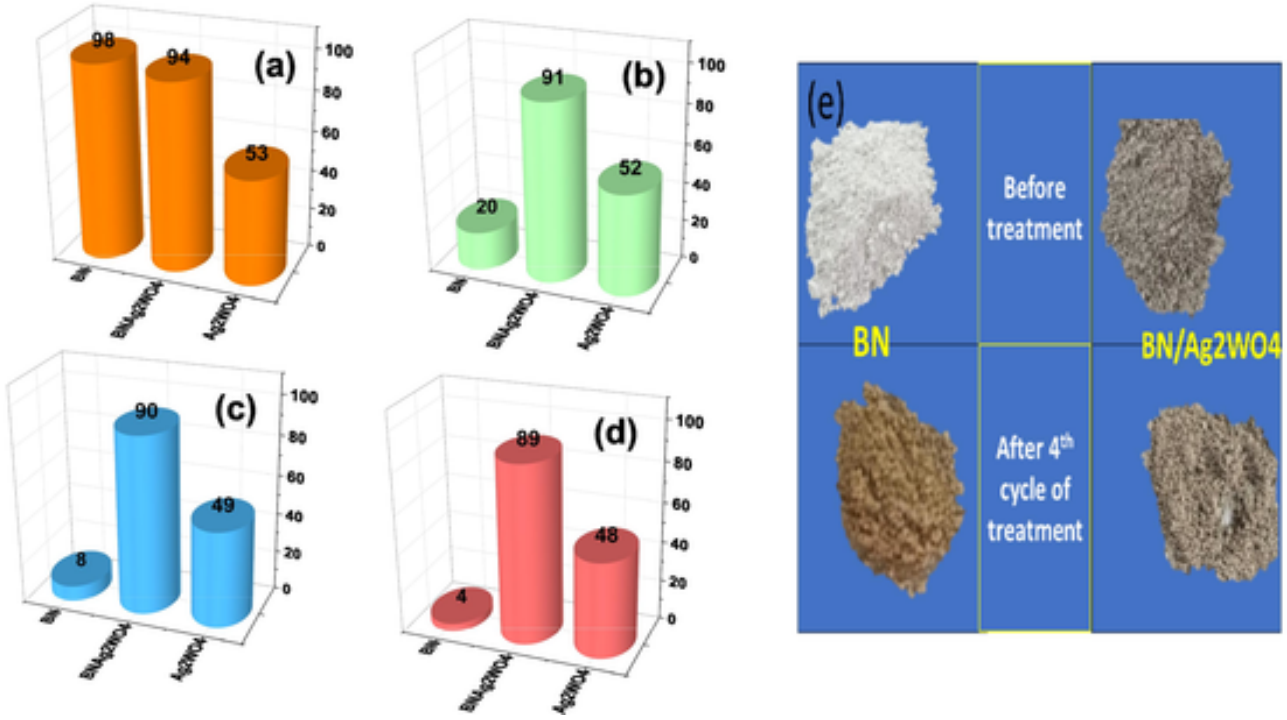

Fig. 7. Photocatalytic efficiency for IC degradation by of BN, Ag_2WO_4 and BN/Ag_2WO_4 nanocomposite for (a) first cycle, (b) second cycle, (c) third cycle and (d) fourth cycle under visible light for 15 mins duration, (e) Boron nitride and BN/Ag_2WO_4 nanocomposite before and after 4 cycles of treatment.

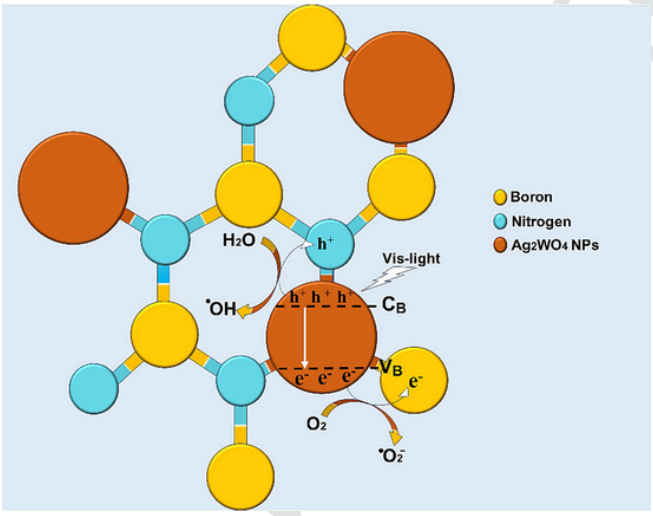

Scheme 2. Plausible mechanism for the degradation of Indigo Carmine dye by BN/Ag_2WO_4nanocomposite.

significant potential for environmental remediation applications as an effective photocatalyst.

Author statement

The work was conceptualized by PM, BYB performed all experiments, including photocatalyst synthesis, characterization, and finalization of the manuscript by PM, ACSCT, and SAI.

Declaration of Competing Interest

The authors declare that they have no known competing financial interests or personal relationships that could have appeared to influence the work reported in this paper.

Data availability

Data will be made available on request.

Acknowledgments

The authors are grateful for the assistance provided by the National Forensic Sciences University.

Appendix A. Supplementary material

Supplementary data to this article can be found online at https://doi.org/10.1016/j.inoche.2023.111560.

References

[1] J. Manzoor, M. Sharma, Impact of textile dyes on human health and environment, in: Impact of Textile Dyes on Public Health and the Environment, IGI Global, 2019, pp. 162–169, doi: 10.4018/978-1-7998-0311-9.ch008.
[2] R. Rashid, I. Shafiq, P. Akhter, & Muhammad, J. Iqbal, M. Hussain, A state-of-the-art review on wastewater treatment techniques: the effectiveness of adsorption method, (n.d.), doi: 10.1007/s11356-021-12395-x/Published.
[3] M.K.H.M. Nazri, N. Sapawe, A short review on photocatalytic toward dye degradation, Mater Today Proc. 31 (2020) A42–A47, doi: 10.1016/j.matpr.2020.10.967.
[4] D. Sudha, P. Sivakumar, Review on the photocatalytic activity of various composite catalysts, Chem. Eng. Process. 97 (2015) 112–133, https://doi.org/10.1016/j.cep.2015.08.006.
[5] W.S. Koe, J.W. Lee, W.C. Chong, Y.L. Pang, L.C. Sim, An overview of photocatalytic degradation: photocatalysts, mechanisms, and development of photocatalytic membrane, Environ. Sci. Pollut. Res. 27 (2020) 2522–2565, https://doi.org/10.1007/s11356-019-07193-5.
[6] M. Saeed, M. Muneer, A. Ul Haq, N. Akram, Photocatalysis: an effective tool for photodegradation of dyes-a review, (n.d.), doi: 10.1007/s11356-021-16389-7/Published.
[7] B.Y. Balarabe, P. Maity, Visible light-driven complete photocatalytic oxidation of organic dye by plasmonic Au-TiO2 nanocatalyst under batch and continuous flow condition, Colloids Surf. A: Physicochem. Eng. Asp. 655 (2022) 130247, https://doi.org/10.1016/J.COLSURFA.2022.130247.
[8] B.Y. Balarabe, S. Bowmik, A. Ghosh, P. Maity, Photocatalytic dye degradation by magnetic XFe2O3 (X: Co, Zn, Cr, Sr, Ni, Cu, Ba, Bi, and Mn) nanocomposites under visible light: a cost efficiency comparison, J. Magn. Magn. Mater. 562 (2022)

169823, https://doi.org/10.1016/J.JMMM.2022.169823.
[9] B. Yaou Balarabe, M.N. Illiassou Oumarou, A.S. Koroney, I. Adjama, A.R. Ibrahim Baraze, Photo-oxidation of organic dye by Fe2O3 nanoparticles: catalyst, electron acceptor, and polyurethane membrane (PU-Fe2O3) effects, J Nanotechnol. 2023 (2023), https://doi.org/10.1155/2023/1292762.
[10] B. Yaou Balarabe, S. Paria, D. Sekou Keita, A.R. Ibrahim Baraze, E. Kalugendo, G.N. Tetteh Tetteh, M. Merycleopha Meringo, M.N. Illiassou Oumarou, Enhanced UV-light active α-Bi2O3 nanoparticles for the removal of methyl orange and ciprofloxacin, Inorg. Chem. Commun. 146 (2022) 110204, https://doi.org/10.1016/J.INOCHE.2022.110204.
[11] A. Trivedi, J. Thakarda, N. Chavda, Y.K. Agrawal, P. Maity, A new route towards selective synthesis of supported Cu2O and CuO nanoparticles under extremely mild condition, Nano-Struct. Nano-Objects 6 (2016) 34–38, https://doi.org/10.1016/j.nanoso.2016.03.004.
[12] B. Agrawal, J. Patel, P. Dave, J. Thakarda, T.S. Anand, P. Maity, Efficient synthesis of a new heterogeneous gold nanocatalyst stabilized by di-alkyne ligand and its applications for photocatalytic dye degradation and transfer hydrogenation reaction, J. Nanopart. Res. 23 (2021), https://doi.org/10.1007/s11051-021-05182-9.
[13] M. Li, N.H. Shah, P. Zhang, P. Chen, Y. Cui, Y. Jiang, Y. Wang, Mechanism, modification and application of silver-based photocatalysts, Mater. Today Sustain. 22 (2023) 100409, https://doi.org/10.1016/J.MTSUST.2023.100409.
[14] Y. Zhang, J. Liu, Y.S. Kang, X.L. Zhang, Silver based photocatalysts in emerging applications, Nanoscale 14 (2022) 11909–11922, https://doi.org/10.1039/d2nr02665a.
[15] Y.V.B. de Santana, J.E.C. Gomes, L. Matos, G.H. Cruvinel, A. Perrin, C. Perrin, J. Andrès, J.A. Varela, E. Longo, Silver molybdate and silver tungstate nanocomposites with enhanced photoluminescence, Nanomater. Nanotechnol. 4 (2014), https://doi.org/10.5772/58923.
[16] C. Liang, S. Qi, S. Mingwang, W. Xianwen, W. Zhengcui, Photoswitches of one-dimensional Ag2, MO4 (M) Cr, Mo, and W), J. Phys. Chem. C 113 (2009) 1764–1768, https://doi.org/10.1021/jp808907e.
[17] Y. Liu, H. Yu, M. Cai, J. Sun, Microwave hydrothermal synthesis of Ag2CrO4 photocatalyst for fast degradation of PCP-Na under visible light irradiation, Catal. Commun. 26 (2012) 63–67, https://doi.org/10.1016/J.CATCOM.2012.04.017.
[18] F. Soofivand, F. Mohandes, M. Salavati-Niasari, Silver chromate and silver dichromate nanostructures: sonochemical synthesis, characterization, and photocatalytic properties, Mater. Res. Bull. 48 (2013) 2084–2094, https://doi.org/10.1016/J.MATERRESBULL.2013.02.025.
[19] Z. Li, X. Chen, Z.L. Xue, Microwave-assisted hydrothermal synthesis of cube-like Ag-Ag 2MoO4 with visible-light photocatalytic activity, Sci. China Chem. 56 (2013) 443–450, https://doi.org/10.1007/s11426-013-4845-5.
[20] M. Feng, M. Zhang, J.M. Song, X.G. Li, S.H. Yu, Ultralong silver trimolybdate nanowires: synthesis, phase transformation, stability, and their photocatalytic, optical, and electrical properties, ACS Nano 5 (2011) 6726–6735, https://doi.org/10.1021/nn202296h.
[21] D.W. Kim, I.S. Cho, S. Lee, S.T. Bae, S.S. Shin, G.S. Han, H.S. Jung, K.S. Hong, Photophysical and photocatalytic properties of Ag2M 2O7 (M = Mo, W), J. Am. Ceram. Soc. 93 (2010) 3867–3872, https://doi.org/10.1111/j.1551-2916.2010.03972.x.
[22] R. Zhang, H. Cui, X. Yang, H. Tang, H. Liu, Y. Li, Facile hydrothermal synthesis and photocatalytic activity of rod-like nanosized silver tungstate, Micro Nano Lett. 7 (2012) 1285–1288, https://doi.org/10.1049/mnl.2012.0765.
[23] X. Liu, J. Hu, J. Li, Y. Hu, Y. Shao, H. Yang, G. Tong, H. Qian, Facile synthesis of Ag2WO4/AgCl nanorods for excellent photocatalytic properties, Mater. Lett. 91 (2013) 129–132, https://doi.org/10.1016/J.MATLET.2012.09.078.
[24] X. Wang, C. Fu, P. Wang, H. Yu, J. Yu, Hierarchically porous metastable β-Ag2WO4 hollow nanospheres: controlled synthesis and high photocatalytic activity, Nanotechnology 24 (2013), https://doi.org/10.1088/0957-4484/24/16/165602.
[25] V.M. Longo, C.C. De Foggi, M.M. Ferrer, A.F. Gouveia, R.S. André, W. Avansi, C.E. Vergani, A.L. Machado, J. Andrés, L.S. Cavalcante, A.C. Hernandes, E. Longo, Potentiated electron transference in α-Ag2WO4 microcrystals with Ag nanofilaments as microbial agent, J. Phys. Chem. A 118 (2014) 5769–5778, https://doi.org/10.1021/jp410564p.
[26] D. Xu, B. Cheng, S. Cao, J. Yu, Enhanced photocatalytic activity and stability of Z-scheme Ag2CrO4-GO composite photocatalysts for organic pollutant degradation, Appl. Catal. B 164 (2015) 380–388, https://doi.org/10.1016/J.APCATB.2014.09.051.
[27] B.Y. Wang, G.Y. Zhang, G.W. Cui, Y.Y. Xu, Y. Liu, C.Y. Xing, Controllable fabrication of α-Ag 2 WO 4 nanorod-clusters with superior simulated sunlight photocatalytic performance, Inorg. Chem. Front. 6 (2019) 209–219, https://doi.org/10.1039/c8qi01025k.
[28] J. Li, F. Liu, Y. Li, Fabrication of an Ag/Ag2MoO4 plasmonic photocatalyst with enhanced photocatalytic performance for the degradation of ciprofloxacin, New J. Chem. 42 (2018) 12054–12061, https://doi.org/10.1039/c8nj02327a.
[29] Z. Zhang, W.Q. Huang, Z. Xie, W. Hu, P. Peng, G.F. Huang, Simultaneous covalent and noncovalent carbon nanotube/Ag3PO4 hybrids: new insights into the origin of enhanced visible light photocatalytic performance, PCCP 19 (2017) 7955–7963, https://doi.org/10.1039/c6cp08853h.
[30] X. Miao, X. Shen, J. Wu, Z. Ji, J. Wang, L. Kong, M. Liu, C. Song, Fabrication of an all solid Z-scheme photocatalyst g-C3N4/GO/AgBr with enhanced visible light photocatalytic activity, Appl. Catal. A 539 (2017) 104–113, https://doi.org/10.1016/J.APCATA.2017.04.009.
[31] S. Zhang, Z. Liu, Y. Zhang, S. Gao, R. Jin, Q. Wang, Highly effective photoelectrochemical performance of solar energy materials based on Ag2WO4-AgX (X = Cl, Br, I) sensitized TiO2 nanotube arrays, Ceram. Int. 44 (2018) 6659–6665, https://doi.org/10.1016/J.CERAMINT.2018.01.077.
[32] Y. Li, R. Jin, X. Fang, Y. Yang, M. Yang, X. Liu, Y. Xing, S. Song, In situ loading of Ag2WO4 on ultrathin g-C3N4 nanosheets with highly enhanced photocatalytic performance, J. Hazard. Mater. 313 (2016) 219–228, https://doi.org/10.1016/J.JHAZMAT.2016.04.011.
[33] B. Singh, G. Kaur, P. Singh, K. Singh, J. Sharma, M. Kumar, R. Bala, R. Meena, S.K. Sharma, A. Kumar, Nanostructured BN-TiO2 composite with ultra-high photocatalytic activity, New J. Chem. 41 (2017) 11640–11646, https://doi.org/10.1039/c7nj02509b.
[34] X. Gao, Y. Yao, X. Meng, Recent development on BN-based photocatalysis: a review, Mater. Sci. Semicond. Process. 120 (2020) 105256, https://doi.org/10.1016/J.MSSP.2020.105256.
[35] G. Cassabois, P. Valvin, B. Gil, Hexagonal boron nitride is an indirect bandgap semiconductor, 2015, doi: 10.1038/nphoton.2015.277.
[36] X. Fu, Y. Hu, Y. Yang, W. Liu, S. Chen, Ball milled h-BN: an efficient holes transfer promoter to enhance the photocatalytic performance of TiO2, J. Hazard. Mater. 244–245 (2013) 102–110, https://doi.org/10.1016/J.JHAZMAT.2012.11.033.
[37] J. Di, J. Xia, M. Ji, B. Wang, S. Yin, Q. Zhang, Z. Chen, H. Li, Advanced photocatalytic performance of graphene-like BN modified BiOBr flower-like materials for the removal of pollutants and mechanism insight, Appl. Catal. B 183 (2016) 254–262, https://doi.org/10.1016/J.APCATB.2015.10.036.
[38] T. Chen, Q. Zhang, Z. Xie, C. Tan, P. Chen, Y. Zeng, F. Wang, H. Liu, Y. Liu, G. Liu, W. Lv, Carbon nitride modified hexagonal boron nitride interface as highly efficient blue LED light-driven photocatalyst, Appl. Catal. B 238 (2018) 410–421, https://doi.org/10.1016/J.APCATB.2018.07.053.
[39] M. Serhan, M. Sprowls, D. Jackemeyer, M. Long, I.D. Perez, W. Maret, N. Tao, E. Forzani, Total iron measurement in human serum with a smartphone, in: AIChE Annual Meeting, Conference Proceedings, American Institute of Chemical Engineers, 2019, https://doi.org/10.1039/x0xx00000x.
[40] X. Fu, Y. Hu, T. Zhang, S. Chen, The role of ball milled h-BN in the enhanced photocatalytic activity: a study based on the model of ZnO, Appl. Surf. Sci. 280 (2013) 828–835, https://doi.org/10.1016/J.APSUSC.2013.05.069.
[41] X.F. Wu, H. Li, Y. Sun, Y.J. Wang, C.X. Zhang, J.Z. Su, J.R. Zhang, F.F. Yang, Y. Zhang, J.C. Pan, Synthesis of SnS2/few layer boron nitride nanosheets composites as a novel material for visible-light-driven photocatalysis, Appl. Phys. A Mater. Sci. Process. 123 (2017), https://doi.org/10.1007/s00339-017-1286-6.
[42] J. Wang, J. Shen, D. Fan, Z. Cui, X. Lü, J. Xie, M. Chen, BN nanosheet: an efficient carriers transfer promoter and stabilizer to enhance the photocatalytic performance of Ag2CO3, Mater. Lett. 147 (2015) 8–11, https://doi.org/10.1016/J.MATLET.2015.01.109.
[43] W. Wu, X. Lv, J. Wang, J. Xie, Integrating AgI/AgBr biphasic heterostructures encased by few layer h-BN with enhanced catalytic activity and stability, J. Colloid Interface Sci. 496 (2017) 434–445, https://doi.org/10.1016/J.JCIS.2017.02.046.
[44] X. Wang, Y. Yang, G. Jiang, Z. Yuan, S. Yuan, A facile synthesis of boron nitride nanosheets and their potential application in dye adsorption, Diam. Relat. Mater. 81 (2018) 89–95, https://doi.org/10.1016/j.diamond.2017.11.012.
[45] R. Guo, X. Qi, X. Zhang, H. Zhang, X. Cheng, Synthesis of Ag2CO3/A-Fe2O3 heterojunction and it high visible light driven photocatalytic activity for elimination of organic pollutants, Sep. Purif. Technol. 211 (2019) 504–513, https://doi.org/10.1016/j.seppur.2018.10.011.
[46] Q. Xu, L. Zhang, J. Yu, S. Wageh, A.A. Al-Ghamdi, M. Jaroniec, Direct Z-scheme photocatalysts: principles, synthesis, and applications, Mater. Today 21 (2018) 1042–1063, https://doi.org/10.1016/j.mattod.2018.04.008.
[47] J.C. Bernède, S. Houari, D. Nguyen, P.Y. Jouan, A. Khelil, A. Mokrani, L. Cattin, P. Predeep, XPS study of the band alignment at ITO/oxide (n-type MoO 3 or p-type NiO) interface, Phys. Status Solidi (A) Appl. Mater. Sci. 209 (2012) 1291–1297, https://doi.org/10.1002/pssa.201127428.
[48] S. Mohammed Harshulkhan, K. Janaki, G. Velraj, R. Sakthi Ganapthy, M. Nagarajan, Effect of Ag doping on structural, optical and photocatalytic activity of tungsten oxide (WO3) nanoparticles, J. Mater. Sci. Mater. Electron. 27 (2016) 4744–4751, https://doi.org/10.1007/s10854-016-4354-3.
[49] R. Wei, Q. Xiao, C. Zhan, Y. You, X. Zhou, X. Liu, Polyarylene ether nitrile and boron nitride composites: coating with sulfonated polyarylene ether nitrile, E-Polymers 19 (2019) 70–78, https://doi.org/10.1515/epoly-2019-0009.
[50] S. Kokilavani, A. Syed, H.A. AL-Shwaiman, M.M. Alkhulaifi, F.N. Almajdhi, A.M. Elgorban, S.S. Khan, Preparation of plasmonic CoS/Ag2WO4 nanocomposites: efficient visible light driven photocatalysts and enhanced anti-microbial activity, Colloids Interface Sci. Commun. 42 (2021), https://doi.org/10.1016/j.colcom.2021.100415.
[51] S. Alam, M.S. Akhtar, E.B. Abdullah, H.S. Kim, S.A. Shin, Planar D-π-A configured dimethoxy vinylbenzene based small organic molecule for solution-processed bulk heterojunction organic solar cells, Appl. Sci. (Switzerland) 10 (2020), https://doi.org/10.3390/APP10175743.
[52] G. Escalante, R. López, F.N. Demesa, G. Villa-Sánchez, V.H. Castrejón-Sánchez, I. Vivaldo de la Cruz, Correlation between Raman spectra and color of tungsten trioxide (WO3) thermally evaporated from a tungsten filament, AIP Adv. 11 (2021), https://doi.org/10.1063/5.0045190.
[53] Q. Guo, Y. Peng, K. Chao, Raman enhancement effect of different silver nanoparticles on salbutamol, Heliyon. 8 (2022), https://doi.org/10.1016/j.heliyon.2022.e09576.
[54] O.Y. Posudievsky, O.A. Khazieieva, V.V. Cherepanov, G.I. Dovbeshko, V.G. Koshechko, V.D. Pokhodenko, Efficient dispersant-free liquid exfoliation down to the graphene-like state of solvent-free mechanochemically delaminated bulk hexagonal boron nitride, RSC Adv. 6 (2016) 47112–47119, https://doi.org/10.1039/c6ra08312a.

[55] M. Du, Y. Wu, X. Hao, A facile chemical exfoliation method to obtain large size boron nitride nanosheets, CrstEngComm 15 (2013) 1782–1786, https://doi.org/10.1039/c2ce26446c.
[56] H. Xu, J. Yan, Y. Xu, Y. Song, H. Li, J. Xia, C. Huang, H. Wan, Novel visible-light-driven AgX/graphite-like C3N4 (X = Br, I) hybrid materials with synergistic photocatalytic activity, Appl. Catal. B 129 (2013) 182–193, https://doi.org/10.1016/J.APCATB.2012.08.015.
[57] Y.D. Premchand, S.A. Suthanthiraraj, Structural investigation of (CuI)0.45–(Ag2WO4)0.55 solid electrolyte using X-ray photoelectron and laser Raman spectroscopies, Electrochem. Commun. 6 (2004) 1266–1269, https://doi.org/10.1016/J.ELECOM.2004.09.026.
[58] F. Zhan, J. Li, W. Li, Y. Liu, R. Xie, Y. Yang, Y. Li, Q. Chen, In situ formation of CuWO4/WO3 heterojunction plates array films with enhanced photoelectrochemical properties, Int. J. Hydrogen Energy 40 (2015) 6512–6520, https://doi.org/10.1016/J.IJHYDENE.2015.03.131.
[59] M. Padervand, K. Gholami, H. Salari, M. Vosoughi, Rapid H2O2-promoted oxidation of anazolene sodium over the [BMIM]PF6/Pt/γ-Al2O3 nanocatalyst, J. Nanostruct. 9 (2019) 489–497. 10.22052/JNS.2019.03.010.
[60] H. Salari, Catalytic Aerobic oxidation of Alkenes by Ag@Metal organic framework with high catalytic activity and selectivity, Phys. Chem. Res. 7 (2019) 701–713. 10.22036/pcr.2019.191018.1646.
[61] J. Shabani Shayeh, H. Salari, Dendritic fibrous nano metal organic framework: a magnetic core-shell structure as high performance material for electrochemical capacitors, J Energy Storage 32 (2020) 101734, https://doi.org/10.1016/J.EST.2020.101734.
[62] H. Salari, J. Shabani Shayeh, A unique 3D structured NiMoO4/MoO3 heterojunction for enhanced supercapacitor performance, Energy Fuel 35 (2021) 16144–16151, https://doi.org/10.1021/acs.energyfuels.1c01793.
[63] H. Salari, M. Kohantorabi, Heterogeneous photocatalytic degradation of organic pollutant in aqueous solutions by S-scheme heterojunction in nickel molybdate nanocomposites, J. Environ. Chem. Eng. 9 (2021) 105903, https://doi.org/10.1016/J.JECE.2021.105903.
[64] H. Salari, Z. Zahiri, Design of S-scheme 3D nickel molybdate/AgBr nanocomposites: tuning of the electronic band structure towards efficient interfacial photoinduced charge separation and remarkable photocatalytic activity, J. Photochem. Photobiol. A Chem. 426 (2022) 113751, https://doi.org/10.1016/J.JPHOTOCHEM.2021.113751.
[65] Y.G. Park, S.N. Nam, M. Jang, C. Min Park, N. Her, J. Sohn, J. Cho, Y. Yoon, Boron nitride-based nanomaterials as adsorbents in water: a review, Sep. Purif. Technol. 288 (2022), https://doi.org/10.1016/j.seppur.2022.120637.
[66] S. Salesi, A. Nezamzadeh-Ejhieh, An experimental design study of photocatalytic activity of the Z-scheme silver iodide/tungstate binary nano photocatalyst, Environ. Sci. Pollut. Res. (2023), https://doi.org/10.1007/s11356-023-29730-z.
[67] K. Vikrant, C.M. Park, K.H. Kim, S. Kumar, E.C. Jeon, Recent advancements in photocatalyst-based platforms for the destruction of gaseous benzene: performance evaluation of different modes of photocatalytic operations and against adsorption techniques, J. Photochem. Photobiol. C: Photochem. Rev. 41 (2019), https://doi.org/10.1016/j.jphotochemrev.2019.08.003.
[68] A. Bathla, S.A. Younis, K.H. Kim, X. Li, TiO2-based catalytic systems for the treatment of airborne aromatic hydrocarbons, Mater. Horiz. (2023), https://doi.org/10.1039/d2mh01583h.
[69] K. Vikrant, K.H. Kim, A. Deep, Photocatalytic mineralization of hydrogen sulfide as a dual-phase technique for hydrogen production and environmental remediation, Appl. Catal. B 259 (2019), https://doi.org/10.1016/j.apcatb.2019.118025.
[70] V. Bharti, K. Vikrant, M. Goswami, H. Tiwari, R.K. Sonwani, J. Lee, D.C.W. Tsang, K.H. Kim, M. Saeed, S. Kumar, B.N. Rai, B.S. Giri, R.S. Singh, Biodegradation of methylene blue dye in a batch and continuous mode using biochar as packing media, Environ. Res. 171 (2019) 356–364, https://doi.org/10.1016/j.envres.2019.01.051.
[71] N. Raza, W. Raza, H. Gul, M. Azam, J. Lee, K. Vikrant, K.H. Kim, Solar-light-active silver phosphate/titanium dioxide/silica heterostructures for photocatalytic removal of organic dye, J. Clean. Prod. 254 (2020), https://doi.org/10.1016/j.jclepro.2020.120031.
[72] W. Li, Q. Wang, L. Huang, Y. Li, Y. Xu, Y. Song, Q. Zhang, H. Xu, H. Li, Synthesis and characterization of BN/Bi2WO6 composite photocatalysts with enhanced visible-light photocatalytic activity, RSC Adv. 5 (2015) 88832–88840, https://doi.org/10.1039/c5ra15417k.
[73] H. Xu, L. Liu, Y. Song, L. Huang, Y. Li, Z. Chen, Q. Zhang, H. Li, BN nanosheets modified WO3 photocatalysts for enhancing photocatalytic properties under visible light irradiation, J. Alloys Compd. 660 (2016) 48–54, https://doi.org/10.1016/j.jallcom.2015.11.042.
[74] M. Nasr, R. Viter, C. Eid, R. Habchi, P. Miele, M. Bechelany, Enhanced photocatalytic performance of novel electrospun BN/TiO2 composite nanofibers, New J. Chem. 41 (2016) 81–89, https://doi.org/10.1039/c6nj03088b.
[75] J. Yan, J. Gu, X. Wang, Y. Fan, Y. Zhao, J. Lian, Y. Xu, Y. Song, H. Xu, H. Li, Design of 3D WO3/h-BN nanocomposites for efficient visible-light-driven photocatalysis, RSC Adv. 7 (2017) 25160–25170, https://doi.org/10.1039/c7ra02929b.
[76] B. Singh, K. Singh, M. Kumar, S. Thakur, A. Kumar, Insights of preferred growth, elemental and morphological properties of BN/SnO2 composite for photocatalytic applications towards organic pollutants, Chem. Phys. 531 (2020), https://doi.org/10.1016/j.chemphys.2019.110659.
[77] S. Shahabuddin, R. Khanam, M. Khalid, N.M. Sarih, J.J. Ching, S. Mohamad, R. Saidur, Synthesis of 2D boron nitride doped polyaniline hybrid nanocomposites for photocatalytic degradation of carcinogenic dyes from aqueous solution, Arab. J. Chem. 11 (2018) 1000–1016, https://doi.org/10.1016/j.arabjc.2018.05.004.
[78] Q. Weng, Y. Ide, X. Wang, X. Wang, C. Zhang, X. Jiang, Y. Xue, P. Dai, K. Komaguchi, Y. Bando, D. Golberg, Design of BN porous sheets with richly exposed (002) plane edges and their application as TiO2 visible light sensitizer, Nano Energy 16 (2015) 19–27, https://doi.org/10.1016/j.nanoen.2015.06.004.
[79] M. Wang, M. Li, L. Xu, L. Wang, Z. Ju, G. Li, Y. Qian, High yield synthesis of novel boron nitride submicro-boxes and their photocatalytic application under visible light irradiation, Catal. Sci. Technol. 1 (2011) 1159–1165, https://doi.org/10.1039/c1cy00111f.
[80] Y. Song, H. Xu, C. Wang, J. Chen, J. Yan, Y. Xu, Y. Li, C. Liu, H. Li, Y. Lei, Graphene-analogue Boron Nitride/Ag 3 PO 4 composite for efficient visible-light-driven photocatalysis, n.d. www.rsc.org/advances.
[81] A. Bumajdad, M. Madkour, Y. Abdel-Moneam, M. El-Kemary, Nanostructured mesoporous Au/TiO2 for photocatalytic degradation of a textile dye: the effect of size similarity of the deposited Au with that of TiO2 pores, J. Mater. Sci. 49 (2014) 1743–1754, https://doi.org/10.1007/s10853-013-7861-0.
[82] T.H. Nguyen, A.T. Vu, V.H. Dang, J.C.S. Wu, M.T. Le, Photocatalytic degradation of phenol and methyl orange with titania-based photocatalysts synthesized by various methods in comparison with ZnO–graphene oxide composite, Top. Catal. 63 (2020) 1215–1226, https://doi.org/10.1007/s11244-020-01361-5.